

Computing Ocean Surface Currents over the Coastal California Current System using 30-minute Lag Sequential SAR Images

Waqas A. Qazi, William J. Emery, *Fellow, IEEE*, Baylor Fox-Kemper

Abstract

As compared to conventional methods of ocean surface currents measurement, spaceborne Synthetic Aperture Radar (SAR) offers cloud-penetrating ocean current observation capability at high spatial resolution. While some studies have shown the potential for using SAR for studying ocean surface currents through feature tracking, they have only analyzed a few images to demonstrate the basic measurement technique, and no concise general technique has been developed. This paper shows the application of the Maximum Cross-Correlation (MCC) method to generate ocean surface currents from nearly 2 years of available sequential spaceborne C-band SAR imagery from the Envisat ASAR and ERS-2 AMI-SAR sensors over the coastal California Current System. The data processing strategies are discussed in detail, and results are compared with High Frequency (HF) radar measured currents. One-dimensional wavenumber spectra of the SAR-derived surface currents agree with the k^{-2} power-law as predicted by submesoscale resolution models. Comparisons with HF radar currents show encouraging results. MCC SAR surface currents are found to have larger magnitudes than the HF radar currents, ≈ 11 cm/s, which may be due to the fact that SAR penetrates only a few cm into the ocean surface while HF radar currents are averaged over the top 1 m of the ocean surface. Along-shore rotation of the currents shows that most of this magnitude difference is contained in the along-shore component, which can be attributed to higher HF radar accuracy in the direct radial cross-shore measurements as

W. A. Qazi and W. J. Emery are with the Department of Aerospace Engineering Sciences, University of Colorado, Boulder, CO, 80309 USA.

B. Fox-Kemper is with the Department of Geological Sciences, Brown University, Providence, RI, 02912 USA.

Manuscript received Monthfullname datenum, year; revised Monthfullname datenum, year. This work was supported by the NASA Physical Oceanography program . W. A. Qazi is partially supported by the Fulbright program. B. Fox-Kemper is supported by NASA NNX09AF38G and NSF 0934737. The SAR images were acquired from ESA under Cat-1 proposal 10009.

compared to lower accuracy in the along-shore components derived from multiple cross-shore radial measurements.

Index Terms

Synthetic aperture radar (SAR), ocean surface currents, remote sensing, sea surface.

I. INTRODUCTION

Ocean surface currents are a significant part of the global ocean circulation and they strongly influence ocean-atmosphere interaction. Coastal surface currents are responsible for surface advection of nutrient-rich waters, which are biologically the richest parts of the oceans [1], thus having a direct impact on the fishing industry. Surface currents are also significant for shipping, navigation, and the analysis and prediction of the spread of pollutants like oil spills. In-situ instruments for measuring ocean surface currents, drifting and moored buoys and ADCPs (Acoustic Doppler Current Profilers), have the disadvantage of being restricted to point measurements only. Drifting buoys can provide a Lagrangian view of the near-surface current but this requires repeated re-seeding of the buoys to comprehensively cover an area. Though effective for current measurement in specific areas of interest, it is prohibitively expensive to routinely and repeatedly deploy in-situ measurement systems in large numbers in all sea conditions. Ground-based coastal HF (High frequency) radar stations can measure high temporal resolution real-time surface currents up to ≈ 180 km off the coast with a spatial resolution of a few kilometers in most weather conditions [2]. However, their coverage is limited to areas near the coast, and furthermore it is difficult to deploy them in remote areas and harsh environments, such as Alaska and the Polar Regions, due to power and maintenance requirements. Radar altimetry is a popular space-based remote sensing method to measure mesoscale current features. However, altimetry measurements can only generate geostrophic currents as the currents are derived by inversion of the altimeter sea surface height estimates [3]. Another major restriction is that radar altimetry cannot function well in shallow waters or near coastlines because of land contamination in the large antenna footprint, tidal variations, and rapid atmospheric variations in coastal waters. Ocean surface currents can also be estimated from thermal infrared (IR) and ocean color (OC) remote sensing imagery by tracking the movement of features through sequential temporal imagery; one popular and effective method used for feature tracking is the Maximum Cross-Correlation

(MCC) method [4], [5]. The MCC method has been successful for AVHRR (Advanced Very High Resolution Radiometer) and MODIS (Moderate-Resolution Imaging Spectroradiometer) thermal IR data as well as OC data from MODIS. However, this method is inhibited by weather because IR and OC data cannot be acquired under cloudy conditions. Furthermore, thermal feature tracking cannot be used in regions where thermal gradients are weak.

Synthetic Aperture Radar (SAR), with its cloud-penetrating, day-night operational capability at a high resolution, typically on the order of a few meters, provides another attractive option for surface current measurement in both the coastal regions and the open ocean. Ocean surface currents can be estimated from SAR imagery by feature tracking in intensity imagery [6], [7], while radial (across-track) currents can be estimated by two methods: through Along-Track Interferometry (ATI) [8], [9] and Doppler centroid tracking [10]. SAR measurements also offer wider coverage in areas inaccessible by in-situ measurement devices, and where cloud cover is very persistent, such as higher latitudes and the tropics. With SAR, surface currents can be mapped over large areas with resolutions typically on the scale of a few km, which are higher than those possible with in-situ methods and most other remote sensing methods.

The microwave range generally used for SAR imaging of the ocean (C-band to X-band) does not penetrate the surface more than a few millimeters, and thus the scattered returns are characteristic of the surface. At intermediate incidence angles (20° - 75°), the primary scattering mechanism is Bragg scattering through small-scale surface capillary waves; however the long-scale waves (primarily wind-driven) also affect the backscatter by influencing the capillary waves through the processes of tilt and hydrodynamic modulation [11]. Biogenic surface slicks associated with fish, upwelling, and phytoplankton blooms generally form monomolecular layers on the sea surface [12]. The effect of these monomolecular slicks is to dampen the surface capillary waves by Marangoni damping, which in turn reduces the Bragg backscatter [13], [14]. Biogenic surface slicks thus appear in SAR imagery as lower backscatter regions, as compared to the surrounding ocean surface. In upwelling zones, SAR imaging of upwelling-related surface slicks may also result due to thermal effects. Increased air stability due to the colder upwelled waters reduces wind stress on the waves, effectively reducing the surface roughness, which leads to lower backscatter [15].

There have been a few published studies exploring feature tracking in SAR intensity imagery for surface current estimation, and they show that surface slicks act as passive tracers for

advection due to surface currents. Lyzenga and Marmorino [6] used feature correlation to track ocean surface slicks imaged by airborne SAR to generate surface currents and current gradients; their results from one single pair of images 20 minutes apart compared well with ADCP currents averaged over 10-20 m depths. Surface currents were estimated in two cases by Liu and Hsu [16] through wavelet feature tracking in Envisat ASAR & ERS-2 SAR datasets, however they didn't compare their results with any other ocean current measurements. In Marmorino *et al.* [7], surface slicks in spiral-eddy convergence zones were tracked to estimate surface currents in a few cases of airborne SAR observations at time separations of around 1.5 hours. More recently, Gade *et al.* [17] compared the results of current generation from feature tracking on both natural and man-made surface slicks (oil spills). Currents were generated using cross-correlation feature tracking on biogenic surface films (ERS-2 SAR and Landsat Thematic Mapper data) and oil spills (Envisat ASAR sequential images). Comparisons with currents generated from a model showed that currents from feature tracking were larger in magnitude, which is attributed to local wind forcing at the sea surface, which is not seen in the model currents which are a mean over the upper-ocean grid point (8 meters in this case).

Ciappa *et al.* [18] have shown that ocean surface currents can also be estimated from SAR intensity images by tracking macro-algae movement through the MCC method. It should be noted that macro-algae blooms, unlike the micro-algae blooms associated with upwelling, form a few-inches thick layer at the sea surface, and appear as a rough and reflective surface.

Previously published work on feature tracking in SAR imagery for estimation of surface currents has been limited to processing and analysis of relatively small and sporadic datasets, and a concise general technique for the same has not been reported. Comparisons with other datasets have been scarce or performed for very specific cases. The research outlined in this paper attempts to fill these gaps by using a semi-automated algorithm with minimal user input to process a large dataset and performing comparisons with ocean currents measured by coast-based HF radar stations. For most of their mission coincidence time frame (2002 - 2011), ESA's Envisat and ERS-2 remote sensing satellites with onboard C-band SAR instruments remained in a specific orbit configuration where ERS-2 followed Envisat in the same orbit with a time-lag of 30 minutes. This small time-lag with their high spatial resolution means these SAR sensors are a unique resource for measurement of ocean surface currents. In the study area, the California Current System (CCS), this 30-minute separation is well-suited for observing

advection of features which exist at submesoscale to mesoscale time and length scales (see Sec. II).

This research study is concerned with the processing of Envisat-ERS2 30-minute lag image pairs acquired over the coastal region in the CCS for 2008-2009. A total of 124 30-minute lag image pairs were processed, and their results and analysis are presented. The paper is organized as follows. Section II delineates the area of study and its characteristics. Section III describes the SAR data used for generating surface currents in this study and also the HF radar data used for comparison and analysis. The MCC method and data processing are discussed in detail in Section IV. The results from data processing are given in Section V. A discussion follows in Section VI, and the paper is summarized in Section VII.

II. STUDY AREA

The California Current System (CCS) is an eastern boundary current system along the US West coast which is well-known for wind-driven upwelling that occurs in the spring-summer (April-August) when surface winds are aligned nearly along-coast, persistently blowing equatorward. The resulting upwelling cold-water filaments can range from submesoscale (1-10 km) to mesoscale (20-100 km) and sometimes grow as large as 200 km [19]. For the purpose of this study, the region of interest in the CCS is the nearshore region of high biological productivity off the US West Coast (up to about 200 km offshore) [20]. The study area is shown in Fig. 1.

The CCS is relatively well understood, and its oceanographic characteristics at the meso- and larger scales are well-known (for a good review, see [19], [21]). The CCS is known to experience high upwelling in the summer due to offshore Ekman transport when surface wind blows southward along the coast or a strong wind stress curl is present [22].

Phytoplankton that rise to the surface during upwelling undergo increased photosynthesis activity at the surface due to better availability of sunlight and increased nutrient availability due to upwelling. The phytoplankton release extra-cellular products, mainly photosynthesis by-products, in the form of biogenic surface slicks; most of these surface slicks are surface-active (surfactants) which adhere and accumulate at the air-sea interface [23].

Besides phytoplankton, which are the primary producers of surface slicks, bacteria, fish, and zooplankton also produce surface slicks. Surface slicks (of any origin) may appear in a convergence zone of an eddy, particularly the submesoscale spiral eddies that appear in the

Southern California Bight. Studies using ERS 1/2 SAR [24] and airborne SAR [7] in the Southern California Bight demonstrate how spiral eddies can be detected through convergence-zone slicks. The study in [24] shows that surfactants can converge within small-scale eddies and delineate sea surface slicks with widths in the range tens to hundreds of meters and lengths greater than 10 km.

The existence of monomolecular surface slicks causes damping of the surface capillary waves through Marangoni damping, which in turn reduces the SAR Bragg backscatter from the ocean surface [14]. The CCS is thus well-known to have features of interest which can be investigated for feature tracking through SAR imagery. Furthermore a large amount of published references of currents and other related variables are available for this region. Currents from coast-based HF radar stations along the California Coast (see Sec. III-B) will be used as reference dataset for comparison with currents generated from SAR through the MCC method.

It is important to consider the balance between biological and physical forcing in the CCS in order to infer current advection from spatial variations in phytoplankton (or chlorophyll, which is an indirect measurement of phytoplankton density), which are sources for surface slicks. It has been well established that in the nearshore region, over time scales of 1-10 days and spatial scales of 25-100 km, phytoplankton behave largely as passive scalars and biological forcing mechanisms play only a marginal role in determining their spatial and temporal distributions [25]. Abbott and Letelier [26] show that in the nearshore region, chlorophyll and SST (sea surface temperature) respond to similar physical forcing, and have identical decorrelation scales. The temporal decorrelation scales of SST and chlorophyll in the CCS are strong functions of spatial scales; length scales of up to 25 km are coupled with time scales of up to 24 hours [25]–[27]. Spatial statistics of SST and chlorophyll are also the same over time scales of 1 day-1 month and spatial scales of 25-100 km [25]. These observations are consistent with the dominance of physical forcing over biological forcing in the nearshore region. In addition to phytoplankton, another manifestation of surface slicks in the CCS is due to small-scale eddies, especially in the Southern California Bight (SCB), which accumulate surface slicks in their convergence zones. Often called spiral eddies, these submesoscale eddies are found at length scales of 10km or less and time scales of less than a day [7], [28].

The CCS has been modeled extensively at grid resolution sufficient to capture submesoscale features. Capet *et al.* [29]–[31] describe simulations of up to 750 m resolution in this location.

A primary result of this work is that the surface velocity field follows a spectral slope (k^{-2}) that is shallower than that predicted by ordinary quasi-geostrophic (QG) theory (k^{-3}), but steeper than that predicted for three-dimensional turbulence and surface quasi-geostrophic (SQG) theory ($k^{-5/3}$). HF radar surface current observations also show agreement with the k^{-2} spectral slope at submesoscale wavenumbers [32]. Capet *et al.* [30] associate this slope with the presence of submesoscale fronts and filaments squeezed between the mesoscale and submesoscale eddies in this region. Capet *et al.* [31] relate these fronts and the distribution of spectral energy with important conclusions about upper-ocean energy cascades. For this reason, we chose to evaluate the spectral slope of our data, to see whether our velocity spectra agree with this important theoretical and modeled result. To date, many of the developments in submesoscale oceanography have been led by theory and modeling without observational validation; the spectra observed from HF radar surface current observations are very recent. It will be shown here that the MCC SAR velocities can be used to directly measure the surface velocity of submesoscale processes.

At the length and time scales in the CCS described above, SAR observations at a resolution of 12.5 m, swath widths of 100 km, and a time separation of 30 minutes, are very suitable for observing surface slick advection due to ocean surface currents.

III. DATA

A. SAR Data

The SAR sensors of interest for this study are the C-band (5.3 GHz) Advanced Microwave Instrument (AMI) SAR onboard ERS-2 and the Advanced SAR (ASAR) onboard Envisat. Both Envisat and ERS-2 were ESA satellites, active, from July, 1995 to July, 2011, and October, 2002 to April, 2012, respectively. For most of their mission coincidence time period, Envisat and ERS-2 flew in the same near-polar, sun-synchronous orbit, with ERS-2 following Envisat by a lag of 30 minutes. Both of these SAR instruments' standard stripmap image mode acquired imagery at a swath width of 100 km and a maximum along-track length of 100 km. The ASAR, however, was an improvement over the ERS AMI SAR instrument in many ways; it featured the standard HH and VV polarization modes along with alternating polarization modes (VV/HH, HV/HH, VH/VV), and it also operated in two ScanSAR modes: the Wide Swath mode with 150 m nominal resolution in azimuth/range and 400 km swath, and the Global Monitoring mode with 1 km nominal resolution in azimuth/range and 400 km swath.

Since we are concerned with feature identification and tracking in SAR backscatter images, so phase-preserved data is not required, rather intensity images are suitable. Archived Image Mode GEC (Ellipsoid Geocoded) SAR datasets from both ASAR and AMI SAR sensors were acquired from ESA. The GEC format is an intensity image format, generated from the raw SAR data using the Range-Doppler algorithm, geolocated and resampled to a map projection, delivered at a pixel sampling of 12.5 m by 12.5 m, with a geometric resolution of approximately 30 m in ground range by 30 m in azimuth. All of these images were acquired in VV-polarization mode, which is better for current mapping purposes than HH-polarization and provides more contrast for the ocean in the presence of a slick (VV-polarization gives higher radar backscatter from the sea surface than HH-polarization [33]). The images were already multi-looked. SAR data processing is described in Section IV-B

B. HF Radar Data

Coast-based High frequency (HF) radar stations measure real-time surface currents in the upper 1 meter of the ocean surface at 0.5 - 6 km horizontal resolution; the coverage zone extends from the near-coast, except for the surfzone, to 50 - 150 km off the coast (depending upon the radar frequency) [32]. The HF range (3 - 30 MHz) is used to receive Bragg backscatter from the surface capillary waves. The Doppler spectrum of the backscatter is used to derive the underlying current that modifies the phase speed of the surface capillary waves [34]. Since the radar backscatter only measures radial velocities, observations from at least two HF radar stations are required for a vector solution. Interpolation techniques are used to convert the radial observations from multiple stations into a two-dimensional surface current field.

High frequency radar stations cover a large portion of the California Coast and give hourly high-temporal resolution data independent of weather conditions. Surface current fields observed from HF radar are available on resampled post-processed grids at both 6 km and 2 km resolutions since 2007 [2]. Hourly 2-km and 6-km grid current fields for 2007-2010 over the California Coastal region have been acquired from the Marine Physical Lab at Scripps Institute of Oceanography.

IV. METHODS

A. *The Maximum Cross-Correlation (MCC) Method*

The MCC method, illustrated in Fig. 2, is an automated procedure that tracks the movements of patterns across sequential images by cross-correlating a pattern template subwindow in an initial image within a specified search window in a second image [4]. The displacement vector between the two sequential images is defined to have its origin at the center of the initial pattern subwindow in the first image and the endpoint at the center of the subwindow location with the maximum cross-correlation in the second image. The velocity vector is calculated using the time separation between the sequential images. The use of MCC for generating ocean surface currents from feature tracking in thermal IR and OC imagery is well-established [5], [35].

One of the requirements for MCC to work well is that the time-separation between the sequential images should not be large enough such that the features being tracked decorrelate significantly. Crocker *et al.* [5] showed that for sequential IR and OC images at 1 km resolution, the MCC method can function well for time separations up to 24 hours between them. Submesoscale features captured by the finer resolution of SAR will evolve on somewhat faster time scales, so the 30 minute separation of the Envisat & ERS-2 configuration is an ideal dataset for this purpose.

The other two main parameters which control the MCC method are the sizes of the template subwindow and the search window. The size of the template subwindow should be large enough to contain enough pixels to define a pattern; however, the larger the subwindow size, the more it smoothes out the structure of the flow. The template subwindow size thus has to be defined keeping in mind a balance between the above two factors. The search window in the second image is set in order to resolve the maximum expected velocity.

A raw velocity field output from the MCC method contains vectors at every grid point, with varying values of cross-correlation. Post-process filtering has to be applied to the raw vector field to get a vector field that depicts the geophysical characteristics of ocean surface currents. As a first step, a minimum correlation cutoff value is used to remove vectors that result from low values of pattern cross-correlation. Vectors associated with single-pixel displacement or having a magnitude larger than a defined threshold value are also removed. Finally, a nearest-neighbor filter is used to ensure spatial coherence. For each grid point in the vector field, the target

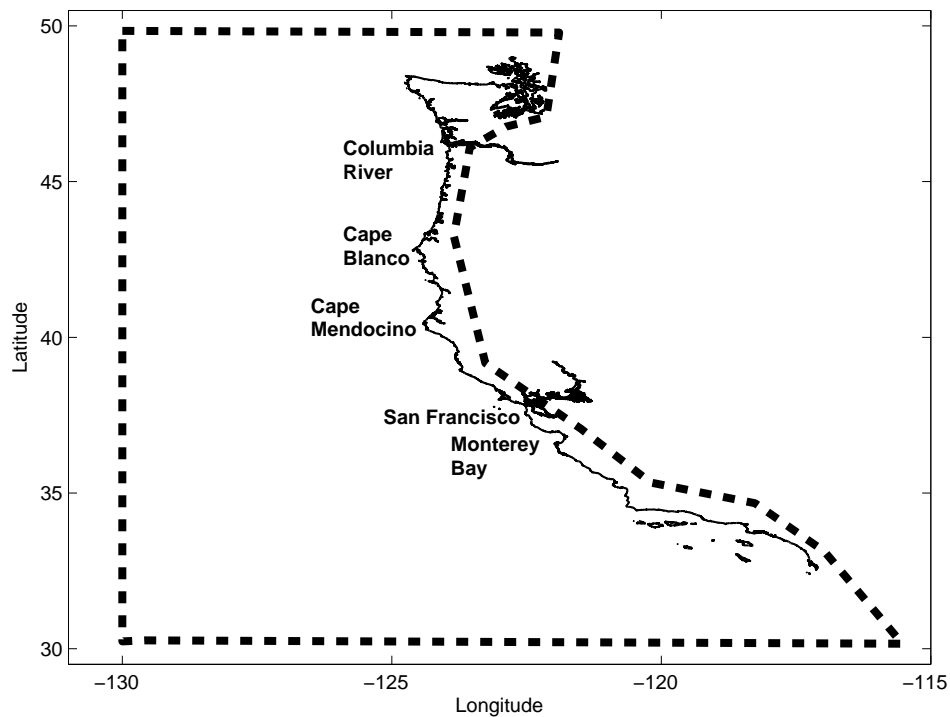


Fig. 1: Study Area. The solid thin line is the US West Coast, the thick dashed line is the study area over which SAR images were acquired.

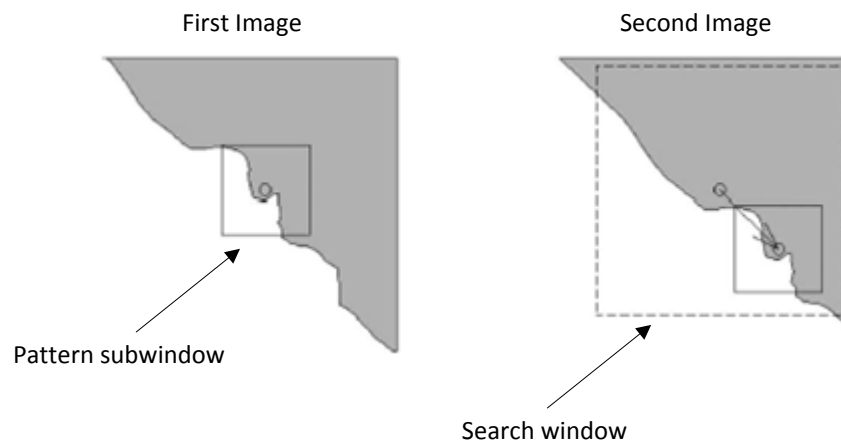


Fig. 2: The Maximum Cross-Correlation (MCC) method. The solid box in the first image is the template subwindow which selects the pattern. This pattern is tracked in the search window (bigger dashed box) in the second image.

vector is compared with all other vectors in its immediate neighborhood. The comparison can be made in many ways, the most common method is to use difference thresholds for u- and v-component magnitudes and direction, and the number of neighborhood vectors violating any of these thresholds is determined. If the number of neighborhood vectors that exceed the defined difference thresholds is greater than a specified limit, the target vector is flagged and discarded. In its common form, the nearest-neighbor filter is thus characterized by the neighborhood size, choice of thresholds for u- and v-components magnitudes, choice of threshold for direction, and choice of the number of neighborhood vectors that must agree to the target vector within these thresholds to keep the target vector.

One important additional step in the processing of thermal IR and OC imagery for MCC is cloud filtering. This is not needed for SAR as clouds are transparent for the microwave range of frequencies used for SAR remote sensing.

B. Data Processing for Generating Currents from 30-minute Lag SAR Images

The data processing chain for the Envisat, ERS-2 30 minute lag image pairs is shown in Fig. 3 as a flowchart. Each processing step is described in detail below. Since the Envisat and ERS-2 SAR intensity images are acquired from two different instruments, they were radiometrically calibrated to normalized backscatter σ^o as a first step.

SAR datasets for both Envisat and ERS-2 are delivered as “scenes” of maximum along-track length of 100 km. This poses a problem when an image “strip” of length > 100 km is ordered from the archive: the image strip is delivered as a sequence of 100 km scenes with some overlap between consecutive scenes. Since the Envisat and ERS2 SAR images do not cover the exact same area on the ground, mosaicking these separate scenes into one image strip is required, for each of Envisat and ERS-2, separately. However, during initial experiments, it was noticed that consecutive scenes in a strip do not have the exact same geolocation, rather there is a “sliding” shift between them in the direction of cross-track imaging; an example of this is shown in Fig. 4.

The magnitude of this slide-shift varies for different strips. The geolocation error due to this slide-shift has to be corrected first before mosaicking the scenes into a single seamless strip. The requisite geolocation correction was performed through image registration. For consistency, the northern-most scene was always chosen as the base image in the geo-registration process. For

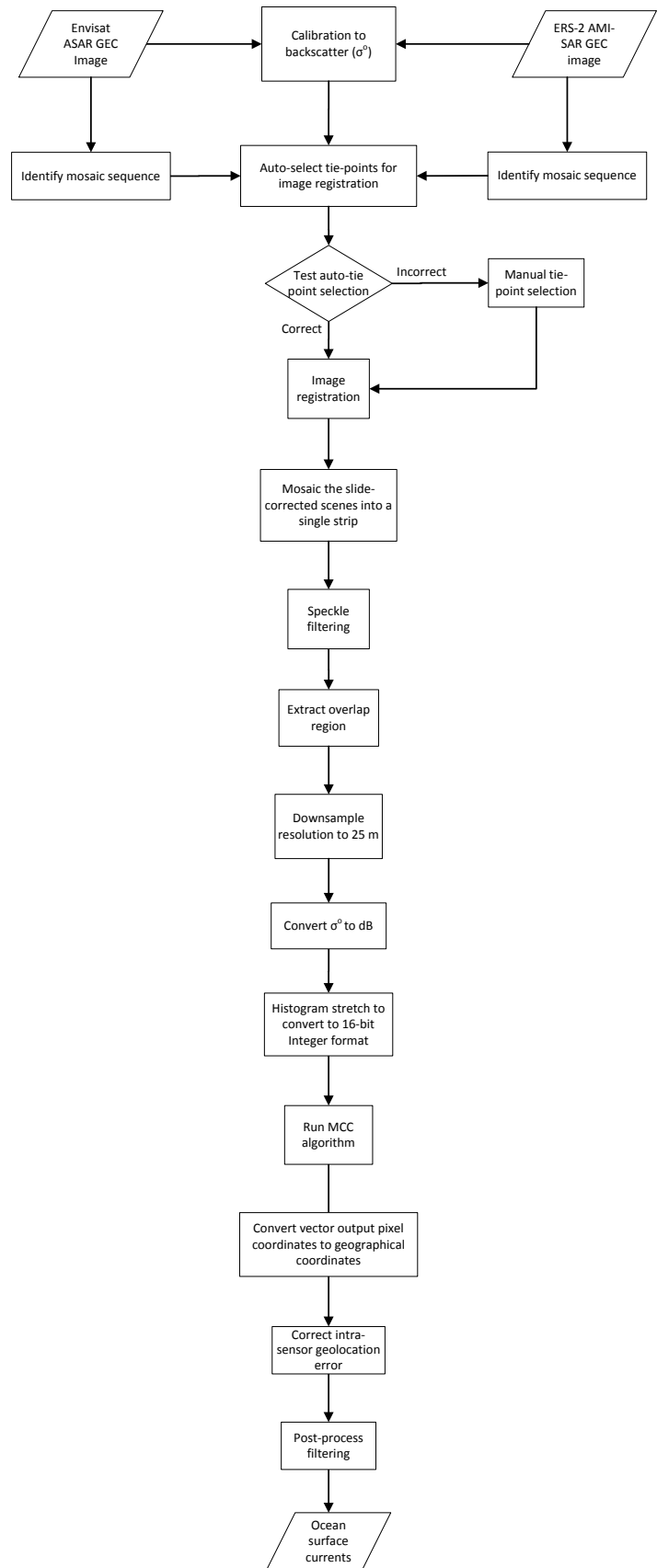


Fig. 3: Data processing flowchart for generating currents from 30-min lag SAR images (see Sec. IV-B for detailed description).

February 15, 2013

DRAFT

strips with more than 2 scenes, a consecutive registration process was used, i.e. the 3rd scene in the strip was registered to the warped 2nd scene as base, the 4th scene in the strip was registered to the warped 3rd scene as base, and so on.

Since the geolocation error between overlap scenes is only a translation due to slide-shift in one direction, and there is no perceptible rotation or skew error, a polynomial of the first degree with bilinear resampling was deemed sufficient for image registration. Automated area-based matching algorithms were used for tie-point selection between the overlapping scenes, which were then used to generate the fit parameters of the one-degree transformation polynomial between the base and warp images.

The automated methods for tie-point selection did not work properly in all cases. An automated procedure for testing the automated tie-point selection and subsequent image registration was developed and manual tie-point selection and registration had to be performed for the cases which failed the test. This testing procedure is described in Section IV-C.

After correcting for the slide-shift in all scenes of the strip, a single seamless strip is generated through mosaicking. Geolocation errors also exist between the Envisat and ERS-2 images, corrections for these are discussed further below.

SAR intensity images have a characteristic “speckle” noise due to the coherent integration of randomly distributed backscatter phase from multiple scatterers within one ground resolution cell. The grainy speckle noise results in a SAR intensity image that does not have a constant mean radiometric level in homogeneous areas. In SAR intensity images, speckle noise has an exponential distribution, and can be statistically modeled as multiplicative noise. Speckle can be reduced at the cost of resolution by “multilook processing” on the Doppler spectrum [36]. Although the SAR intensity images were already multi-looked, there was still significant speckle noise in the images. Spatial filters were used to further suppress speckle: successive Lee, Median, Median (3 x 3 pixels) were applied to preserve edges while smoothing.

The mosaicked speckle-filtered Envisat and ERS-2 image strips were then spatially subset to the region of mutual coverage. For ease in data handling and faster processing, the images were downsampled at this point by a factor of 2, from the native 12.5 m resolution to 25 m resolution.

In the calibrated σ^0 image, ocean has low backscatter values in general, and the features of interest are at even lower backscatter due to damping effects (Sec I). It is useful to increase the contrast of these low intensity values; this is done through applying a dB transformation, at the

cost of decreasing the overall dynamic range in the image. It should be noted here that pixels in SAR intensity data have a negative exponential probability distribution, with a mean equal to variance. A dB transformation standardizes the variance, i.e. variance becomes constant and independent of the mean [37].

At this point in the processing chain, the SAR images were stored in single-precision (32-bit floating point) format. The legacy MCC program, however, takes data input only in 16-bit integer format. The processed SAR images were thus converted at this stage to 16-bit integer format through linear histogram stretching.

The MCC program was run with a maximum velocity threshold of 60 cm/s for the search window. High-velocity jets in the CCS are known to achieve velocities in excess of 50 cm/s [19]; Crocker *et al.* [5] used a maximum velocity threshold of 70 cm/s for defining the search window for running MCC on IR and OC imagery. We ran a few datasets using two different maximum velocity limits of 60 cm/s and 70 cm/s. In the case of 70 cm/s velocity threshold, there were only a few vectors generated with magnitude higher than 60 cm/s, and most of them were discarded during post-process filtering. The velocity threshold of 60 cm/s was chosen as a constant value for processing all datasets. For a pixel resolution of 25 m and a time separation of 30 minutes, this corresponded to a search box of 75 x 75 pixels. The pattern subwindow size was chosen to be 1.1 km x 1.1 km (44 x 44 pixels), adequate enough to track the features that exist in the range of tens of meters up to 2-3 km, yet small enough to not smooth out the fine-resolution during pattern matching. Thus, the resolution of the MCC velocity field will be less than the 25 m SAR images (1-2 km is chosen here).

The MCC program takes the input integer-format sequential images as 2-D arrays and the output vectors are given in terms of pixel coordinates. Using the map projection information attached with the input images, the pixel coordinates were converted to geographic coordinates (longitude and latitude). The output grid resolution of the current fields was 1.87 km.

The slide-shift geolocation error between consecutive scenes in the same strip and its correction was described above. Besides that, there is also a slide-shift error between the Envisat and ERS-2 images. The correction for this intra-sensor slide-shift depends upon the number of scenes in the image strip for each sensor. In the simpler case where the image strips for both Envisat and ERS-2 are composed of only one scene each, this geolocation error can be treated simply as a uni-directional slide-shift between the two images. The input images to the MCC algorithm

are not land-masked, and ideally the cross-correlation over land should not show any movement vectors over the time-period of 30 minutes. Any vectors over land are thus a depiction of the geolocation error between the two sensors. Experiments indicated that the vector magnitudes are nearly constant over land, with some outlying vectors near the image edges and coast-ocean boundaries. The intra-sensor geolocation error in this case is corrected by first calculating the overall mean of the shift vectors over land and then removing this mean value from the ocean current vectors. Note that while calculating the mean shift, vectors near the coast-ocean boundary are ignored, along with any vectors that are statistical outliers (any vectors outside 1.5 standard deviation range, calculated from the total set of vectors over land).

The intra-sensor geolocation error correction gets more complicated when either or both of Envisat and ERS-2 strips have multiple scenes: every scene in each strip is on a slightly different geolocation grid. Assuming that image registration during the mosaicking process for each strip is accurate enough, the overall mean shift vectors over land should give a shift vector close to the true shift vectors between every pixel in the overlap region of the two sensors. While calculating the mean shift vector over land, the same pruning process is used as in the case of single-image strip: vectors near the coast-ocean boundary and vectors that are statistical outliers (vectors that fall outside the 1.5 standard deviation limit) are ignored. Due to the underlying assumption above, the accuracy of the geolocation correction for mosaicked strips depends upon the accuracy of the image registration in the mosaicking process.

The raw MCC output vectors fields were post-processed using the filters described in Section IV-A. The cross-correlation minimum cut-off was set at 0.2; this was an empirical value decided by experimenting with a few sample cases. Vectors associated with single-pixel displacement and a maximum velocity of 60 cm/s were removed. The nearest-neighbor filter was used with a neighborhood size of 5 x 5 grid points, with the target vector at the center grid point. The direction difference threshold was set at 60° and the u- and v-component difference thresholds were set at 0.8 times target vector u- and v-component magnitudes, respectively. If more than 3 neighborhood vectors violated any of the above thresholds, the target vector was discarded. Post-process filtering is the final step in the processing chain.

C. Procedure for Testing Automated Tie-Point Selection and Registration

As mentioned in Sec. IV-B, an automated procedure for testing tie-point selection and subsequent image registration prior to scene mosaicking in a strip needs to be devised. This procedure was developed based on the MCC algorithm, and is shown in Fig. 5 as a flowchart. For any two consecutive scenes in the strip which need to be geo-registered, the auto-tie point algorithm is run with different settings. If the auto tie-point algorithm gives unrealistic values of points (e.g. sometimes the top-left corner in both images is erroneously chosen as a tie-point), then the images are not registered, and manual tie-point selection is required in this case.

In the other case, when realistic tie-points are chosen, the images are registered using the selected tie-points, subset to their overlap area, downsampled to 25 m resolution, transformed to dB, and converted to 16-bit integer format through histogram stretching. These images now cover only the overlap area between the consecutive scenes. To check for geolocation errors in these subset images, the MCC algorithm is run over them, with a pattern subwindow size of 25 x 25 pixels and a search window size of 50 x 50 pixels; these window sizes are chosen as a balance between efficient processing and assumptions regarding expected maximum geolocation errors. A time-separation value of 1 sec is used, so that the output vectors effectively give the shift vectors in cm units.

The raw vectors from the MCC algorithm are filtered at a minimum cross-correlation coefficient threshold of 0.3. If the MCC vectors are non-existent or have zero values above the 0.3 cross-correlation threshold, this indicates that the images have been properly geo-registered. If the number of non-zero MCC vectors is more than 10 % of the total number of vectors, that means there is a possibility of georegistration error. In this case, the vectors are filtered again by removing outliers (vectors that fall outside the 1.5 standard deviation range), and the overall mean of the filtered vectors is calculated. This overall mean vector is a quantitative measure of the geolocation error in cm. This can easily be converted into the 25 m pixel georegistration error.

A summary of these parameters is generated, which identifies the multi-scene strips which need manual tie-point selection and geo-registration.

V. RESULTS

Each Envisat-ERS2 30-min lag image pair was processed independently, with the final results being the post-processed ocean surface current vectors. An example of surface current generation from one pair is shown in Fig. 6. Envisat and ERS-2 strips for this case were comprised of two scenes each. The mosaicked Envisat and ERS-2 σ^o [dB] strips are shown in Fig. 6a and Fig. 6b, respectively. These images are speckle-filtered, subset to their mutual overlap region, and downsampled to 25 m resolution. The ERS-2 image lags the Envisat image by 30 minutes. Some ocean feature changes can be seen between the two images, however this is clearer in the difference image in Fig. 6c, especially in the regions to the west of Santa Catalina Island. The dark linear features in region A seem to have shifted position as a group in the two images, as evident from the alternating increase and decrease pattern seen in Fig. 6c. Region B also depicts change in intensity, however this is more of a homogenous change over a relatively large region, and is not due to advection; the actual cause of this change may be changes in wind patterns, or atmosphere/ocean fronts. Due to the MCC pattern subwindow and search window size definitions, intensity changes of the kind depicted in region B, which might not be due to ocean surface advection, are automatically ignored for the most part. This can be seen in the raw MCC vector field in Fig. 6d: there are few vectors over region B. The raw vector field shows a nearly-constant vector flow over land, this is due to the intra-sensor geolocation error (see Sec. IV-B). Fig. 6e shows the vector field after correction for this geolocation error. The final vector output after post-process filtering is shown in Fig. 6f; notice the elimination of vectors that appear spurious and spatially incoherent, and what appears to be a small-scale eddy in the top left corner of Region B. Note that the vector fields shown in Fig. 6d and 6e have been filtered at a cross-correlation threshold of 0.2 for display.

A. Wavenumber Spectra

The wavenumber spectrum of ocean currents gives an insight into the kinetic energy distribution in the ocean over a range of spatial scales. Recently, there has been great interest in the use of wavenumber spectra to analyze energy distributions over the meso to submeso scales. Wavenumber spectra of surface velocity over the global ocean were calculated for the geostrophic case by Stammer [38] using satellite altimeter data; however that analysis was restricted to length scales of 100 km and above as altimeter signals become dominated by noise below length scales

of ≈ 100 km. In the CCS, there is substantial velocity variance that resides in the submesoscale range. Capet *et al.* [29], [31] derived currents from a high-resolution numerical model of the CCS, and were able to derive wavenumber spectra in the submesoscale range down to 1.5 km. Kim *et al.* [32] used HF radar currents to estimate the wavenumber spectra in the CCS; the high resolution of the HF radar current fields allowed for derivation of wavenumber spectra at length scales as small as 2 km.

In the submesoscale wavenumber regime, theory predicts a power-law decay behavior; current traditional quasigeostrophic (QG) theory specifies a power-law slope of -3 [39], so called "surface quasigeostrophic theory (SQG)" and 3D isotropic turbulence theory predicts a power-law slope of $-5/3$ [40], [41], and high-resolution simulations and frontogenesis theory predicts a slope of -2 [29], [31]. The submesoscale wavenumber spectra derived over the CCS using a high-resolution CCS model [29], [31] and HF radar currents [32] both show very good agreement with the k^{-2} power law.

The MCC SAR currents generated at a base resolution of ≈ 1.87 km should capture submesoscale phenomena well, and wavenumber spectra from them should also show agreement with the power law decay. The wavenumber spectrum calculated for the KE in MCC SAR currents is shown in Fig. 7, along with the 95 % confidence limits and relevant power-law spectrum slopes: the k^{-2} slope is reproduced, with appropriate magnitude, from Fig. 1 in Capet *et al.* [31] while the $k^{-5/3}$ and k^{-3} slopes are arbitrary.

Each current field calculated from a 30-min lag image pair was re-gridded and interpolated to a constant 1.9 km resolution field. One-dimensional KE spectra were calculated over these 2-km re-gridded vectors along the x-direction (each line of constant latitude); prior to this, each row was conditioned by a Hann window. All of these 1-D spectra from one current field were then averaged together to generate a mean spectrum for one field. The mean KE spectrum for each field was band-averaged to increase the 95 % confidence interval. Out of the total 124 processed 30-min lag image pairs, only 96 current fields were used for the wavenumber spectral analysis; other pairs either had no or less than 15 vectors, or did not produce enough vectors after re-gridding and interpolation to a 1.9 km grid. The mean KE spectrum shown in Fig. 7 was produced by taking an overall mean of the individual mean spectra from each current field.

The MCC SAR vectors seem to follow the k^{-2} power law in the wavenumber range of 10^{-4} rad/m to 10^{-3} rad/m, in excellent agreement with the kinetic energy spectrum from the model

of Capet et al. [31]. The slightly different behavior in the wavenumber range $<10^{-4}$ rad/m may be due to the fact that the 1.9 km interpolation grid is set up over the minimum and maximum distance from the shore present in each derived currents field. Since the features of interest, surface slicks, predominantly exist close to the coast, the probability of detecting vectors gets less as distance from the coast increases. At the same time, all spectra are calculated at a fixed wavenumber resolution and length (by zero-padding during spectra calculation) to achieve constant wavenumbers for all cases for calculating the means. Both of these factors combine to cause larger interpolation errors in the spectra calculation in regions farther from the coast. On the whole, the KE wavenumber spectrum in Fig. 7 indicates consistency between SAR MCC velocities and actual geophysical ocean current signals in the CCS.

B. Comparison with HF Radar Currents

Coast-based High frequency (HF) radar stations are rapidly developing into an observational tool for ocean surface currents over the US West Coast for the last few years. There have been quite a few validation studies which show their general agreement with other current measurements, ranging from 1 to 19 cm/s (see [32] for a good summary). High frequency radar measured currents are a unique resource in that they measure surface currents in the coastal zone at high spatial and temporal resolutions, which are difficult to achieve using other methods.

High frequency radar currents datasets over the US California Coast are available at two different spatial resolutions: 2 km and 6 km. MCC currents derived from SAR are compared with both 2 km and 6 km resolution HF radar currents separately. Before comparison, the HF radar currents were filtered at a normalized uncertainty threshold of 0.8 for both u- and v-components [2]. MCC SAR currents were re-gridded to 2 km and 6 km resolutions for comparison with the HF radar datasets at the same resolution. After re-gridding, any MCC SAR grid points which were at a distance of greater than half the grid resolution from the original grid points were omitted from further analysis. Also, any interpolated grid points which did not have both MCC SAR and HF radar current vectors were omitted from further analysis. The HF radar current fields at an hourly temporal resolution were composited by linear weighting (following the method in Chubb et al. [42]) to bring them to the same time span as the MCC SAR currents. Some sample plots of re-gridded MCC SAR and HF radar vectors are shown for both the 2 km and 6 km resolution case in Fig. 8. The vector fields in each plot are scaled together to the same reference

vector. Both MCC SAR and HF radar vectors show the same general circulation, however some disagreements can also be seen in these sample plots.

To quantitatively compare the two datasets, their residuals were calculated and analyzed. In Fig. 9 we show the histograms of residuals for magnitude and direction (anti-clockwise from East) for 2 km HF radar currents subtracted from re-gridded 2 km MCC SAR currents (Fig. 9a, 9b) and for 6 km HF radar currents subtracted from re-gridded 6 km MCC SAR currents (Fig. 9c, 9d). Mean and standard deviation values for each set of residuals are also noted. The residuals for both 2 km and 6 km resolutions are quite symmetric about the mean, are unimodal, and show some agreement to the estimated normal histograms. The magnitude residuals have a significant non-zero mean, ≈ 11 cm/s, for both 2 and 6 km resolutions; the direction residuals have a wide bias but the means are close to 0. This can be interpreted as showing that MCC SAR currents agree overall with the HF radar currents in identifying current vector direction, but have higher magnitudes than HF radar currents. Possible reasons for this are discussed in Sec. VI.

In Fig. 10 we show the histograms of residuals for u-component (zonal component) and v-component (meridional component) for 2 km (Fig. 10a, 10b) and 6 km resolutions (Fig. 10c, 10d) as in Fig. 9. The thick black lines are the normal histograms estimated from the mean and variance in the respective residuals. Mean and standard deviation values for each set of residuals are also noted. The residuals for both 2 km and 6 km resolutions are quite symmetric about the mean, are unimodal, and show some agreement to the estimated normal histograms. The means for the u- and v-component residuals are non-zero, positive, and have approximately the same values. For both 2 km and 6 km resolutions, this can be interpreted as showing that the increased magnitude in MCC SAR currents is distributed somewhat evenly in both the u- and v-components.

Since the area of study is in the near-shore region, it would be interesting to examine the along- and cross-shore components of the current fields. The along- and cross-shore rotation is performed by an anti-clockwise rotation of 45° . In Fig. 11 we present the histograms of the residuals for the along- and cross-shore components of the MCC SAR and HF radar vector fields, calculated in the same way as Fig. 10. Fig. 11a and 11b show the residuals for the 2 km resolution while Fig. 11c and 11d show the residuals for the 6 km resolution. The histograms are again unimodal and symmetrical about the mean, and show some agreement to the estimated normal histograms. However, for both the 2 km and 6 km resolutions, a marked difference can be observed between the means: the means for the cross-shore components are close to 0 while

the means for the along-shore components have a significant positive value (≈ 7 cm/s). It seems that the cross-shore component has very good agreement while the along-shore component has higher magnitudes for MCC SAR. It should be noted here that the actual velocity measurements of HF radar stations are only cross-shore radial velocities, and radial velocities from two or more HF radar stations are used to acquire a full 2-D vector solution, where each radial measurement is considered to be a linear combination of the full 2-D vector current components [2]. This process of conversion of multiple measured radials to a 2-D vector imparts higher errors to the interpolated along-shore component as compared to the directly observed cross-shore component. It seems that MCC SAR currents have good agreement with the higher accuracy cross-shore HF radar components, while the MCC SAR along-shore components have higher magnitudes than the lower accuracy along-shore HF radar components.

VI. DISCUSSION

The physical mechanism for imaging of surface slicks in SAR intensity images has been described in Sec. I. There are, however, certain conditions under which surface slicks cannot be seen by SAR. One important factor in SAR backscatter from the ocean surface is wind. If the wind speed is too low, there is not enough capillary wave action on the surface, which reduces backscatter. In this case the Bragg backscatter is small in magnitude, so even an ocean surface without slicks would appear as low-backscatter. On the other hand, strong winds make the ocean surface rougher, which would cause the low backscatter from a slick over the ocean surface to be contaminated with high backscatter. Thus, surface slick imaging from SAR is affected by both low and high winds. In general, the chances of SAR detection of biogenic surface slicks on the ocean surface decrease with increasing wind speed: higher wind speed causes higher waves, removing surface films from the sea surface through wave breaking processes and upper layer mixing [33], [43]. The lower wind speed threshold for biogenic surface slick detection in SAR is not well-known, while the higher wind speed threshold has been noted to be in the range of 6-7 m/s [44], [45].

Low-backscatter signatures in SAR intensity images may also occur due to rain, wave-current interactions, conditions in the marine atmospheric boundary layer, and oil slicks [43], [46]. These sources of low-backscatter are generally ignored in the processing of sequential SAR imagery of 30-min lag because of the defined MCC processing parameters, which focuses on surface slick

accumulation and advection. However, the MCC processing does not explicitly employ any other mechanism to distinguish between low-backscatter features from different phenomena; this could be a future improvement in the method to make it more robust. Also, due to the above-mentioned phenomena, it is not always possible to detect surface slicks in SAR imagery even if they exist on the surface. These restrictions limit the use of the MCC method for current detection in SAR images.

The geolocation errors in a multi-scene strip and between the two sensors, described in Sec. IV-B, play an important role in defining the absolute accuracy of the estimated currents. The correction for intra-sensor geolocation errors indirectly depends upon the accuracy of the image registration process during strip mosaicking for each sensor. For the mosaic slide-shift geolocation error, preliminary analysis with a few image pairs shows that after correction, residual geolocation errors have a maximum range of 4-6 pixels. For 12.5 m pixel resolution, this amounts to a 50-75 m displacement error, and an absolute velocity error of ± 2.77 to ± 4.16 cm/s for the 30-min lag image pairs. These errors are ignored in the processing at this time. It is planned in the future to derive uncertainty measures from these errors for the currents derived from each SAR image pair.

While HF radar currents serve as a good reference dataset for MCC SAR currents due to their coincident coverage at comparable resolution, the direct comparisons done here should be accompanied by a note of caution. While C-band SAR penetrates, at most, only a few cm into the ocean surface, the HF radar currents being used are measured and averaged over the top 1 m of the ocean surface [2]. In fact, this could be the reason why MCC SAR currents show greater magnitudes than HF radar currents in general. Under ideal steady-state wind near the ocean surface, the Ekman spiral is set up in the first few meters depth in the ocean. In the Ekman spiral, the current vectors change direction and experience a reduction in magnitude with depth. This would imply that the magnitude of the 1 m averaged HF radar average currents will be less than MCC SAR currents measured at the surface. Gade *et al.* [17] reported the same higher magnitude in currents derived from SAR feature tracking when they compared their derived currents with model currents averaged over the top 4 m of the ocean, and they too attributed it to the effect of surface wind. While this is only a hypothesis and a probable explanation for the higher-magnitude of currents in SAR, we expect to explore this further by analyzing surface wind fields along with the SAR images. The conjecture is that higher velocity winds would

set up a stronger vertical shear in the Ekman layer and should show higher difference between MCC SAR currents and HF radar currents. A correlation between wind speed and disagreement between the two current fields would be one affirmation of this conjecture.

Another factor that should be kept in mind is Stokes drift due to short-scale surface gravity waves which induce a net flow in their direction of propagation. The contribution of this drift would be present in surface slicks tracked in 30-min separation SAR image pairs. The hourly-averaged surface current measurements by HF radar should also contain the effect of Stokes drift, but the impact of this drift measured by HF radar would depend on the waves resonant to the radar frequency. Hence, the MCC SAR method and HF radar could measure different Stokes drift contributions in their total current velocity measurements. The contribution of Stokes drift to total surfactant velocity is a topic of present research (e.g. [47], McWilliams, J. C. and Fox-Kemper, B., Oceanic wave-balanced surface fronts and filaments, submitted to *J. Fluid Mech.*, 2012).

VII. SUMMARY

The initial results from MCC processing on sequential 30-min lag SAR images from Envisat ASAR and ERS-2 AMI C-band SAR sensors over nearly 2 years show that ocean surface currents can be generated from tracking surface slicks in SAR over the coastal CCS (California Current System). We discuss in detail the data processing techniques used for deriving currents from sequential SAR imagery. This general method can be applied to various kinds of sequential SAR data by adjusting different parameters.

Wavenumber spectra calculated from the derived currents seem to follow k^{-2} power-law, in agreement with high-resolution models and frontogenesis theory, and show that the derived currents depict actual geophysical signals in the CCS. Comparisons with HF radar currents of both 2 km and 6 km resolution show promise: the residuals are uni-modal and symmetric about the mean. The MCC SAR currents appear to be greater in magnitude, by ≈ 11 cm/s, than HF radar currents in general, while the direction agreements are reasonable. Transformation into cross- and along-shore components shows that nearly all of this magnitude difference is contained in the along-shore component, while the magnitudes of the cross-shore components are closely in agreement with each other. This could be explained by the fact that the cross-shore radials are directly measured by HF radar stations while the along-shore component is interpolated from

multiple radial observations. The comparisons with HF radar, however, should be considered with a note of caution as C-band SAR penetrates only a few cm into the ocean surface, while HF radar currents are averaged over the top 1 m of the ocean surface.

In the future, we plan to undertake further detailed analyses of the MCC SAR currents and implementing comparisons with HF radar which would take into account the difference in their measurements depths. Other plans include comparisons with other methods of surface current measurement from SAR (Along-track interferometry and Doppler centroid methods).

ACKNOWLEDGMENT

The authors would like to thank Jeffrey Thayer and Scott Palo for their valuable input and ideas. Nathan Longbotham and Fabio Pacifici are thanked for their scrutiny of the the manuscript. Ibraheem Khan is thanked for help with processing vector files. The authors would also like to acknowledge partial support from the NASA Physical Oceanography program as part of the OST Science Team.

REFERENCES

- [1] J. H. Ryther, "Photosynthesis and fish production in the sea." *Science*, vol. 166, no. 3901, pp. 72–76, Oct. 1969.
- [2] S. Y. Kim, E. J. Terrill, and B. D. Cornuelle, "Mapping surface currents from HF radar radial velocity measurements using optimal interpolation," *Journal of Geophysical Research*, vol. 113, no. C10, pp. 1–16, Oct. 2008.
- [3] W. J. Emery, D. G. Baldwin, and D. K. Matthews, "Sampling the mesoscale ocean surface currents with various satellite altimeter configurations," *IEEE Transactions on Geoscience and Remote Sensing*, vol. 42, no. 4, pp. 795–803, Apr. 2004.
- [4] W. J. Emery, A. C. Thomas, M. J. Collins, W. R. Crawford, and D. L. Mackas, "An objective method for computing advective surface velocities from sequential infrared satellite images," *Journal of Geophysical Research*, vol. 91, no. C11, pp. 12 865–12 878, 1986.
- [5] R. I. Crocker, D. K. Matthews, W. J. Emery, and D. G. Baldwin, "Computing Coastal Ocean Surface Currents From Infrared and Ocean Color Satellite Imagery," *IEEE Transactions on Geoscience and Remote Sensing*, vol. 45, no. 2, pp. 435–447, Feb. 2007.
- [6] D. R. Lyzenga and G. O. Marmorino, "Measurement of surface currents using sequential synthetic aperture radar images of slick patterns near the edge of the Gulf Stream," *Journal of Geophysical Research*, vol. 103, no. C9, pp. 18 769–18 777, 1998.
- [7] G. O. Marmorino, B. Holt, M. J. Molemaker, P. M. DiGiacomo, and M. A. Sletten, "Airborne synthetic aperture radar observations of spiral eddy slick patterns in the Southern California Bight," *Journal of Geophysical Research*, vol. 115, no. C5, pp. 1–14, May 2010.
- [8] R. M. Goldstein and H. A. Zebker, "Interferometric radar measurement of ocean surface currents," *Nature*, vol. 328, no. 20, pp. 707–709, 1987.

- [9] R. Romeiser, S. Suchandt, H. Runge, U. Steinbrecher, and S. Grunler, "First Analysis of TerraSAR-X Along-Track InSAR-Derived Current Fields," *IEEE Transactions on Geoscience and Remote Sensing*, vol. 48, no. 2, pp. 820–829, Feb. 2010.
- [10] B. Chapron, F. Collard, and F. Ardhuin, "Direct measurements of ocean surface velocity from space: Interpretation and validation," *Journal of Geophysical Research*, vol. 110, no. C7, pp. 1–17, 2005.
- [11] G. R. Valenzuela, "Theories for the interaction of electromagnetic and oceanic waves ? A review," *Boundary-Layer Meteorology*, vol. 13, no. 1-4, pp. 61–85, Jan. 1978.
- [12] W. Alpers, V. Wismann, R. Theis, H. Hühnerfuss, N. Bartsch, J. Moreira, and J. D. Lyden, "The damping of ocean surface waves by monomolecular sea slicks measured by airborne multi-frequency radars during the SAXON-FPN experiment," in *[Proceedings] IGARSS'91 Remote Sensing: Global Monitoring for Earth Management*, vol. 4. IEEE, 1991, pp. 1987–1990.
- [13] W. Alpers and H. Hühnerfuss, "The Damping of Ocean Waves by Surface Films: A New Look at an Old Problem," *Journal of Geophysical Research*, vol. 94, no. C5, pp. 6251–6265, 1989.
- [14] V. Botte and D. Mansutti, "Numerical modelling of the Marangoni effects induced by plankton-generated surfactants," *Journal of Marine Systems*, vol. 57, no. 1-2, pp. 55–69, Aug. 2005.
- [15] P. Clemente-Colón and X.-H. Yan, "Observations of East Coast upwelling conditions in synthetic aperture radar imagery," *IEEE Transactions on Geoscience and Remote Sensing*, vol. 37, no. 5, pp. 2239–2248, 1999.
- [16] A. K. Liu and M.-K. Hsu, "Deriving Ocean Surface Drift Using Multiple SAR Sensors," *Remote Sensing*, vol. 1, no. 3, pp. 266–277, Jul. 2009.
- [17] M. Gade, B. Seppke, and L. Dreschler-Fischer, "Mesoscale surface current fields in the Baltic Sea derived from multi-sensor satellite data," *International Journal of Remote Sensing*, vol. 33, no. 10, pp. 3122–3146, May 2012.
- [18] A. Ciappa, L. Pietranera, A. Coletta, and X. Jiang, "Surface transport detected by pairs of COSMO-SkyMed ScanSAR images in the Qingdao region (Yellow Sea) during a macro-algal bloom in July 2008," *Journal of Marine Systems*, vol. 80, no. 1-2, pp. 135–142, Feb. 2010.
- [19] D. M. Checkley and J. A. Barth, "Patterns and processes in the California Current System," *Progress In Oceanography*, vol. 83, no. 1-4, pp. 49–64, Dec. 2009.
- [20] S. A. Henson and A. C. Thomas, "Phytoplankton scales of variability in the California Current System: 2. Latitudinal variability," *Journal of Geophysical Research*, vol. 112, no. C7, p. C07018, Jul. 2007.
- [21] R. J. Lynn and J. J. Simpson, "The California Current System: The seasonal variability of its physical characteristics," *Journal of Geophysical Research*, vol. 92, no. C12, pp. 12 947–12 966, 1987.
- [22] M. H. Pickett and J. D. Paduan, "Ekman transport and pumping in the California Current based on the U.S. Navy's high-resolution atmospheric model (COAMPS)," *Journal of Geophysical Research*, vol. 108, no. C10, pp. 1–10, 2003.
- [23] V. Žutić, B. Čosović, E. Marčenko, N. Bihari, and F. Kršinić, "Surfactant production by marine phytoplankton," *Marine Chemistry*, vol. 10, no. 6, pp. 505–520, Dec. 1981.
- [24] P. M. DiGiacomo and B. Holt, "Satellite observations of small coastal ocean eddies in the Southern California Bight," *Journal of Geophysical Research*, vol. 106, no. C10, pp. 22 521–22 543, 2001.
- [25] K. L. Denman and M. R. Abbott, "Time scales of pattern evolution from cross-spectrum analysis of advanced very high resolution radiometer and coastal zone color scanner imagery," *Journal of Geophysical Research*, vol. 99, no. C4, p. 7433, 1994.
- [26] M. R. Abbott and R. M. Letelier, "Decorrelation scales of chlorophyll as observed from bio-optical drifters in the California Current," *Deep Sea Research Part II: Topical Studies in Oceanography*, vol. 45, no. 8-9, pp. 1639–1667, Aug. 1998.
- [27] T. M. Powell, C. V. W. Lewis, E. N. Curchitser, D. B. Haidvogel, A. J. Hermann, and E. L. Dobbins, "Results from a

- three-dimensional, nested biological-physical model of the California Current System and comparisons with statistics from satellite imagery,” *Journal of Geophysical Research*, vol. 111, no. C7, p. C07018, 2006.
- [28] C. J. Bassin, L. Washburn, M. A. Brzezinski, and E. McPhee-Shaw, “Sub-mesoscale coastal eddies observed by high frequency radar: A new mechanism for delivering nutrients to kelp forests in the Southern California Bight,” *Geophysical Research Letters*, vol. 32, no. 12, p. L12604, 2005.
- [29] X. Capet, J. C. McWilliams, M. J. Molemaker, and A. F. Shchepetkin, “Mesoscale to Submesoscale Transition in the California Current System. Part I: Flow Structure, Eddy Flux, and Observational Tests,” *Journal of Physical Oceanography*, vol. 38, no. 1, pp. 29–43, Jan. 2008.
- [30] —, “Mesoscale to Submesoscale Transition in the California Current System. Part II: Frontal Processes,” *Journal of Physical Oceanography*, vol. 38, no. 1, pp. 44–64, Jan. 2008.
- [31] —, “Mesoscale to Submesoscale Transition in the California Current System. Part III: Energy Balance and Flux,” *Journal of Physical Oceanography*, vol. 38, no. 10, pp. 2256–2269, Oct. 2008.
- [32] S. Y. Kim, E. J. Terrill, B. D. Cornuelle, B. Jones, L. Washburn, M. A. Moline, J. D. Paduan, N. Garfield, J. L. Largier, G. Crawford, and P. M. Kosro, “Mapping the U.S. West Coast surface circulation: A multiyear analysis of high-frequency radar observations,” *Journal of Geophysical Research*, vol. 116, no. C3, pp. 1–15, Mar. 2011.
- [33] W. Alpers and H. A. Espedal, “Oils and surfactants,” in *Synthetic Aperture Radar Marine User’s Manual*, C. R. Jackson and J. R. Apel, Eds. Washington, D. C.: National Oceanic and Atmospheric Administration, 2004, ch. 11, pp. 263–275.
- [34] H. C. Graber, D. R. Thompson, and R. E. Carande, “Ocean surface features and currents measured with synthetic aperture radar interferometry and HF radar,” *Journal of Geophysical Research*, vol. 101, no. C11, pp. 25 813–25 832, 1996.
- [35] M. M. Bowen, W. J. Emery, J. L. Wilkin, P. C. Tildesley, I. J. Barton, and R. Knewton, “Extracting multiyear surface currents from sequential thermal imagery using the maximum cross-correlation technique,” *Journal of Atmospheric and Oceanic Technology*, vol. 19, no. 10, pp. 1665–1676, 2002.
- [36] J. C. Curlander and R. N. McDonough, *Synthetic Aperture Radar: Systems and Signal Processing*. Wiley-Interscience, 1991.
- [37] C. Oliver and S. Quegan, *Understanding Synthetic Aperture Radar Images*. SciTech Publishing, 2004.
- [38] D. Stammer, “Global Characteristics of Ocean Variability Estimated from Regional TOPEX/POSEIDON Altimeter Measurements,” *Journal of Physical Oceanography*, vol. 27, no. 8, pp. 1743–1769, Aug. 1997.
- [39] P. Y. Le Traon, P. Klein, B. L. Hua, and G. Dibarboure, “Do Altimeter Wavenumber Spectra Agree with the Interior or Surface Quasigeostrophic Theory?” *Journal of Physical Oceanography*, vol. 38, no. 5, pp. 1137–1142, May 2008.
- [40] P. Klein, B. L. Hua, G. Lapeyre, X. Capet, S. Le Gentil, and H. Sasaki, “Upper Ocean Turbulence from High-Resolution 3D Simulations,” *Journal of Physical Oceanography*, vol. 38, no. 8, pp. 1748–1763, Aug. 2008.
- [41] X. Capet, P. Klein, B. L. Hua, G. Lapeyre, and J. C. McWilliams, “Surface kinetic energy transfer in surface quasigeostrophic flows,” *Journal of Fluid Mechanics*, vol. 604, pp. 165–174, May 2008.
- [42] S. R. Chubb, R. P. Mied, C. Y. Shen, W. Chen, T. E. Evans, and J. Kohut, “Ocean Surface Currents From AVHRR Imagery: Comparison With Land-Based HF Radar Measurements,” *IEEE Transactions on Geoscience and Remote Sensing*, vol. 46, no. 11, pp. 3647–3660, Nov. 2008.
- [43] J. Svejksky and J. Shandley, “Detection of offshore plankton blooms with AVHRR and SAR imagery,” *International Journal of Remote Sensing*, vol. 22, no. 2-3, pp. 471–485, Jan. 2001.
- [44] T. Hamre and H. A. Espedal, “Operational use of wind data for slick detection,” in *3rd ERS Symp. on Space at the Service of our Environment*, Florence, 1997, pp. 1417–1421.

- [45] P. Pavlakis, D. Tarchi, and A. J. Sieber, "On the monitoring of illicit vessel discharges using spaceborne SAR remote sensing - a reconnaissance study in the Mediterranean sea," *Annals OF Telecommunications*, vol. 56, no. 11-12, pp. 700–718, 2001.
- [46] H. A. Hovland, J. Johannessen, and G. Digranes, "Slick detection in SAR images," in *Proceedings of IGARSS '94 - 1994 IEEE International Geoscience and Remote Sensing Symposium*, vol. 4. IEEE, 1994, pp. 2038–2040.
- [47] F. Ardhuin, L. Marié, N. Rasclé, P. Forget, and A. Roland, "Observation and Estimation of Lagrangian, Stokes, and Eulerian Currents Induced by Wind and Waves at the Sea Surface," *Journal of Physical Oceanography*, vol. 39, no. 11, pp. 2820–2838, Nov. 2009.

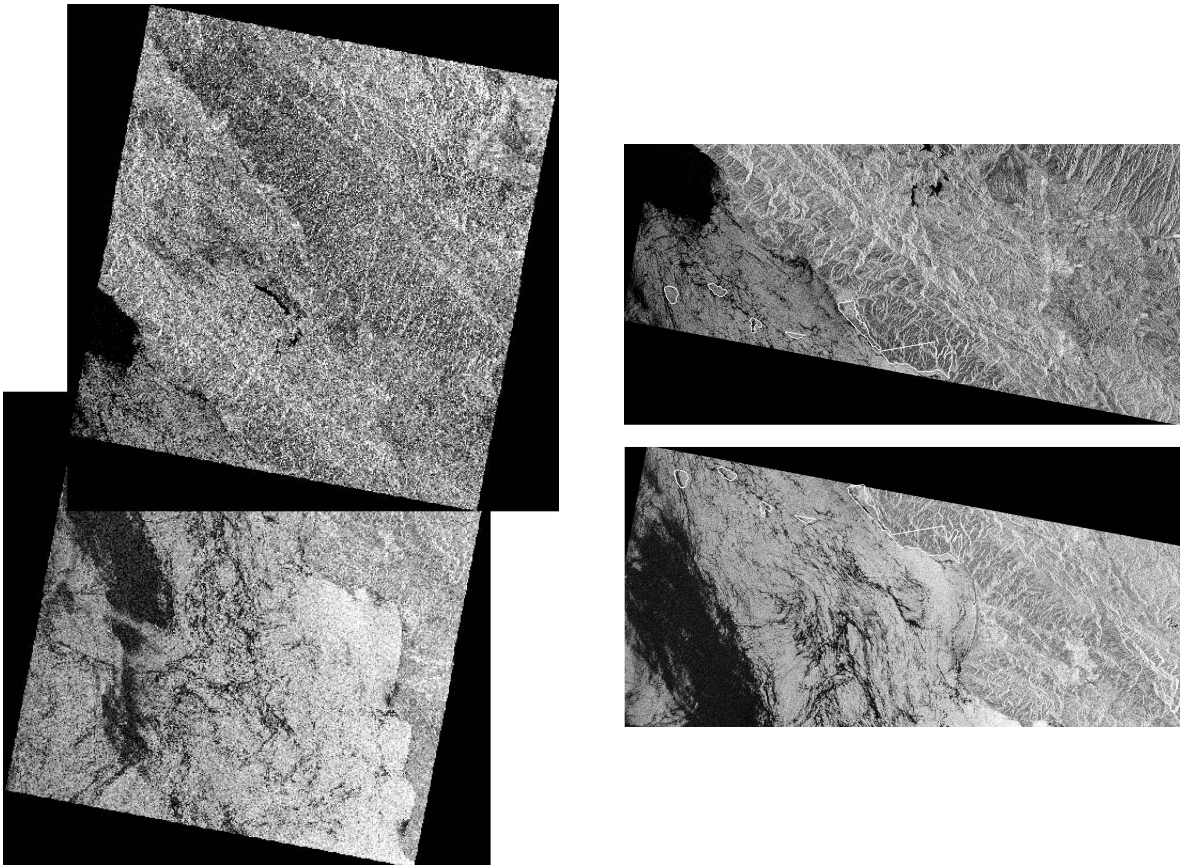


Fig. 4: Example of the slide-shift geolocation error between overlapping scenes in a single strip. An Envisat ASAR strip comprised of two scenes is shown in the left panel, calibrated to σ^0 and converted to dB for visualization. The right panel shows a zoomed in view of the overlap region of the two scenes; the white polygons represent a vector overlay tied to the coordinates of the northern (top) image.

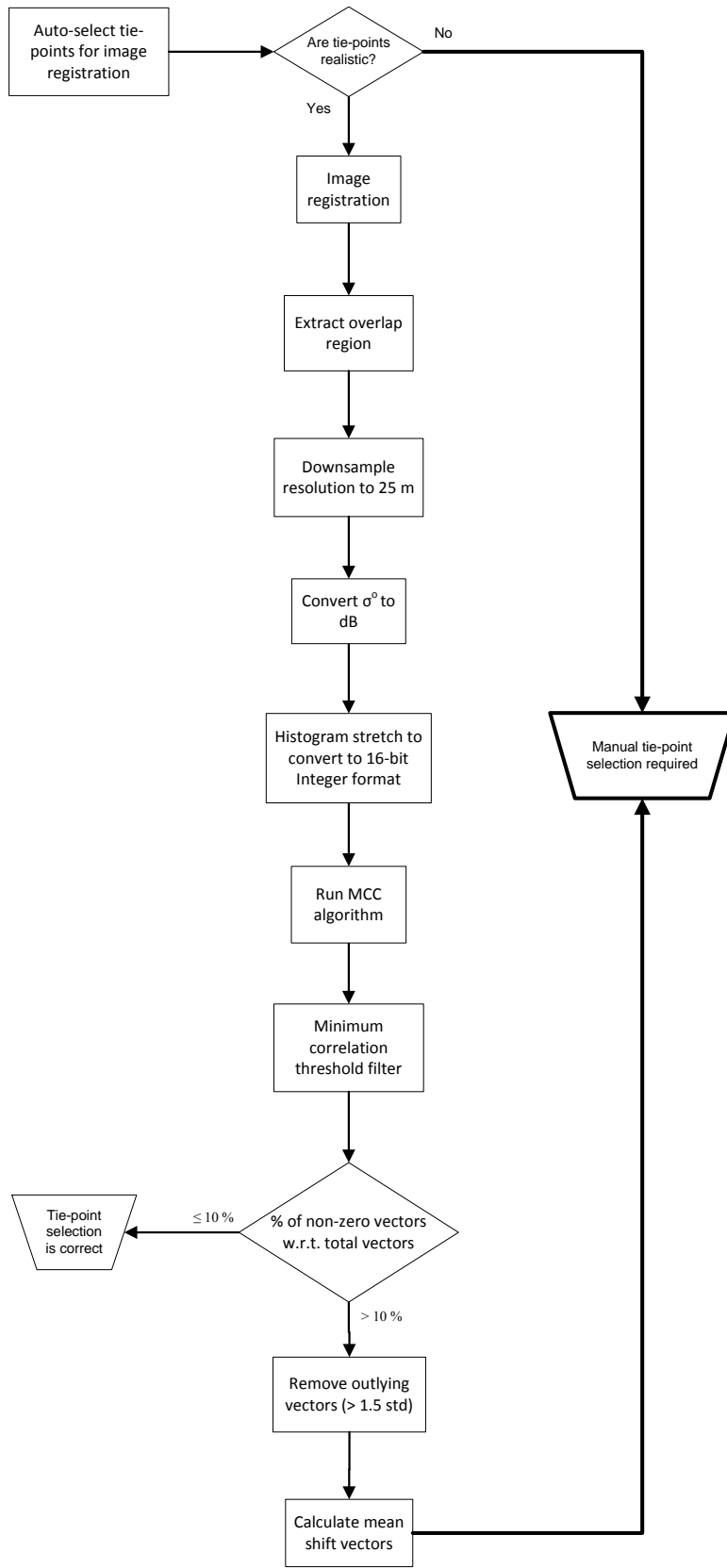


Fig. 5: Data processing flowchart for testing automated tie-point selection and image registration (see Sec. IV-C for detailed description).

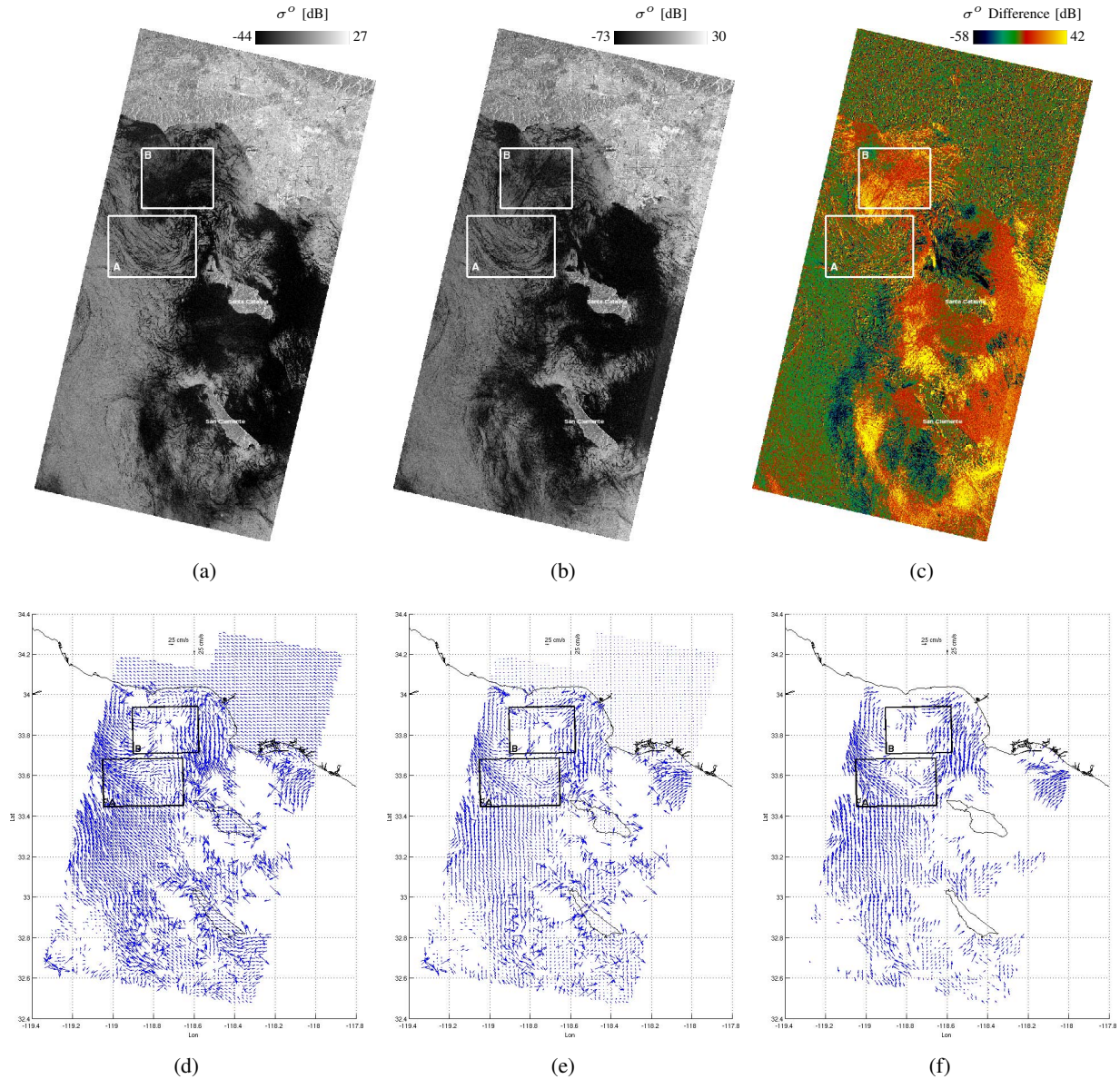


Fig. 6: Sample case of Envisat-ERS2 30-min lag image pair processing. (a) and (b) show the calibrated σ^o [dB] Envisat and ERS images, respectively. The difference image [dB] is shown in (c). (d) shows the raw MCC current field derived from the SAR image pair in (a) and (b), filtered at a cross-correlation coefficient threshold of 0.2. (e) shows the result after intra-sensor geolocation error correction. The final output vector field after post-process filtering is shown in (f).

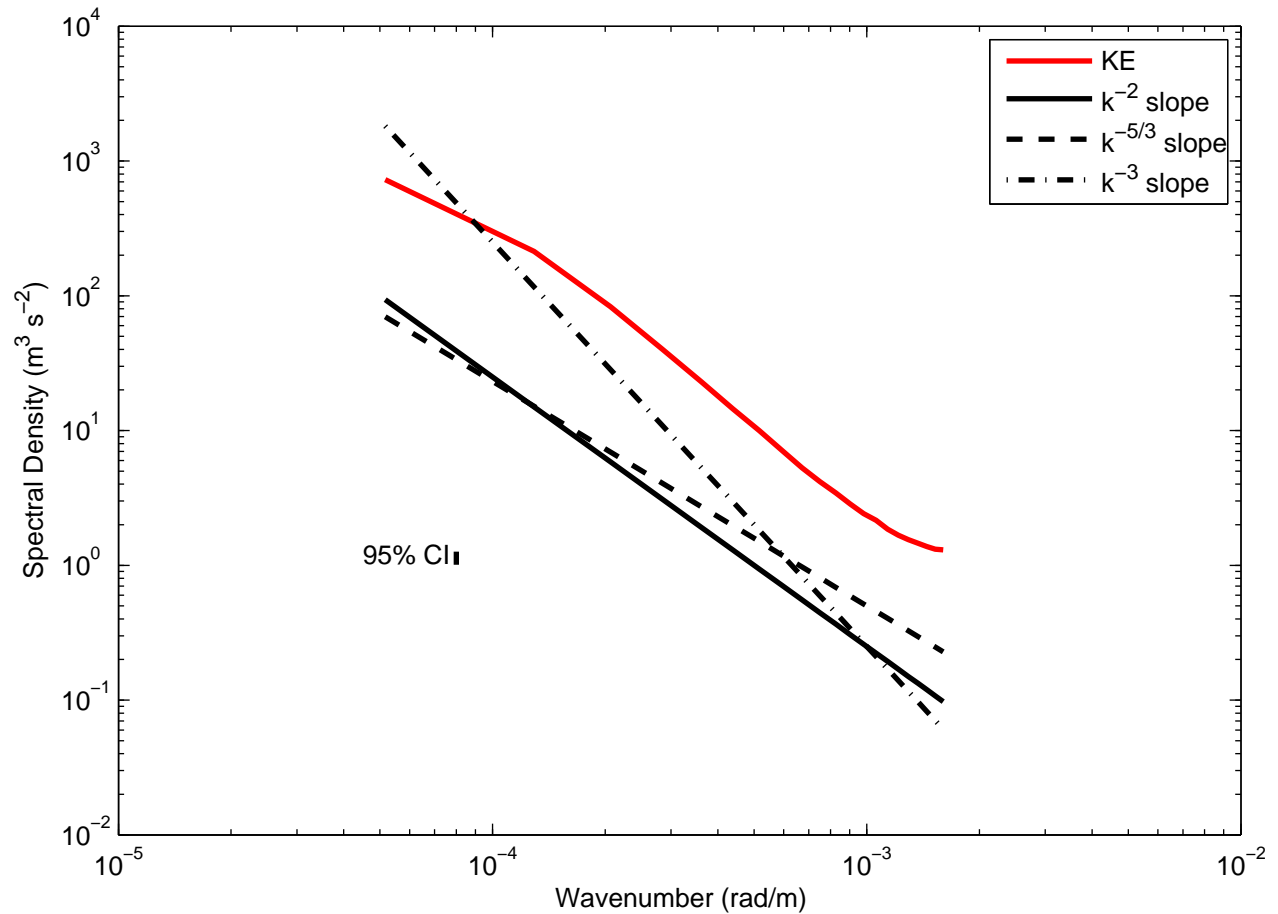


Fig. 7: Mean KE wavenumber spectrum for MCC SAR currents, averaged over a number of different times and scenes as described in the text. Various power-law slopes are also shown. The k^{-2} slope is reproduced, with appropriate magnitude, from Fig. 1 in Capet et al. [31] while the $k^{-5/3}$ and k^{-3} slopes are arbitrary.

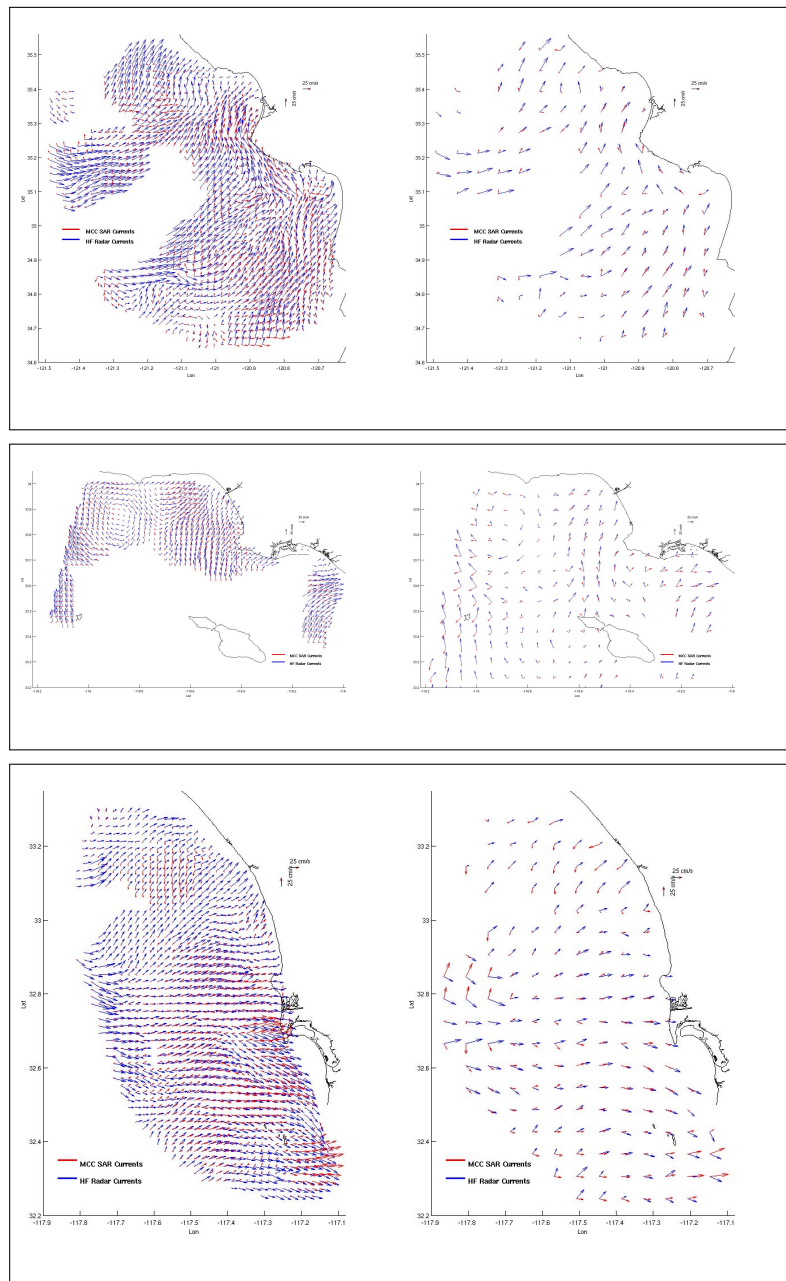


Fig. 8: Some sample plots of the MCC SAR vectors re-gridded to the overlapping HF radar datasets of 2 km (plots on the left) and 6 km (plots on the right) resolutions. The top, middle, and bottom panel each show processed MCC SAR vectors over different regions, along with the HF radar vectors. In each plot, the vectors are scaled to the same reference vector.

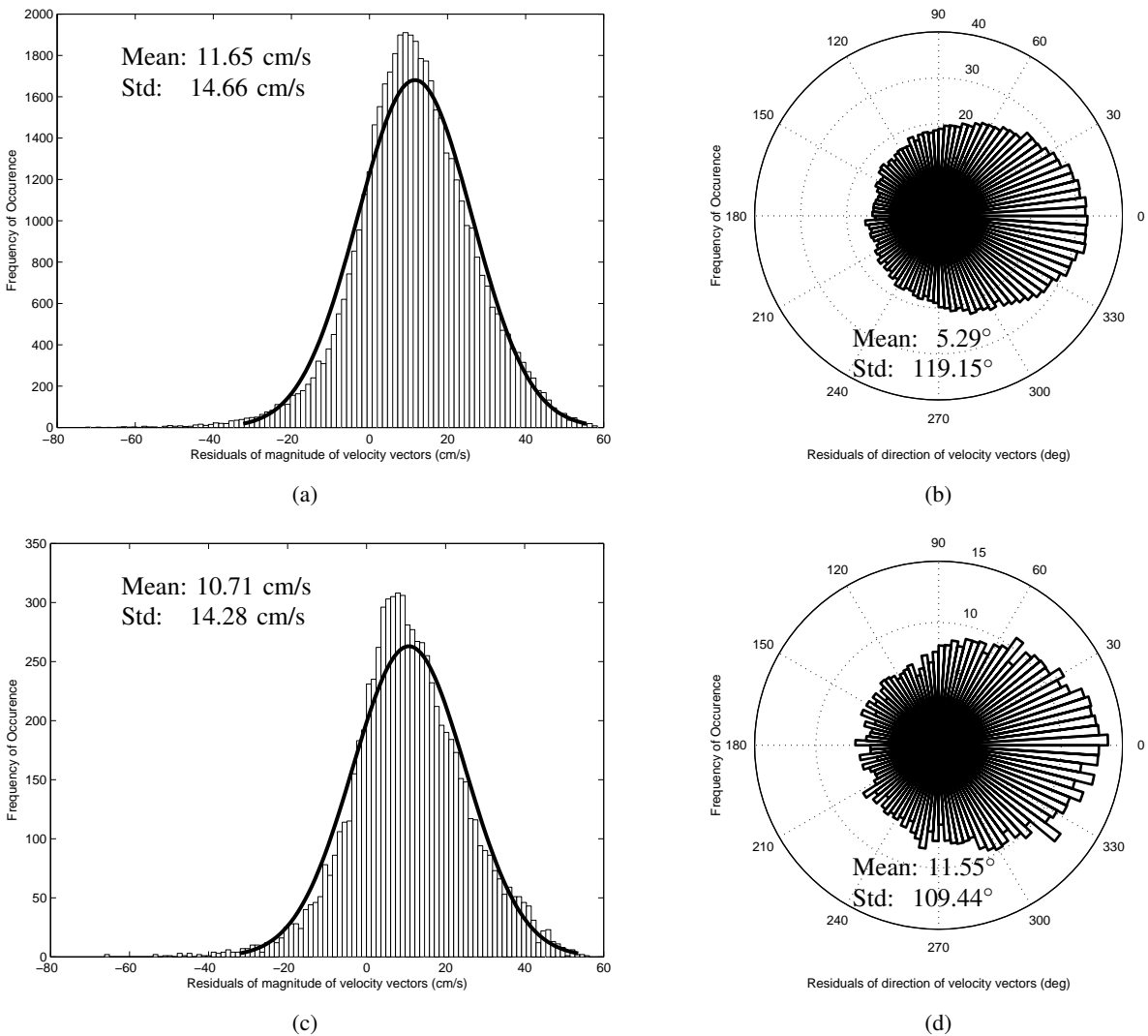


Fig. 9: Histograms of residuals for magnitude and direction of re-gridded MCC SAR currents. The top row is for the 2 km resolution HF radar currents, while the bottom row is for 6 km resolution HF radar currents. (a) and (c) are residual histograms for magnitude, (b) and (d) are residual histograms for direction (anti-clockwise from East). The thick black lines in (a) and (c) are the normal histograms estimated from the mean and variance in the respective residuals. The mean and standard deviation for each case is indicated in the plots.

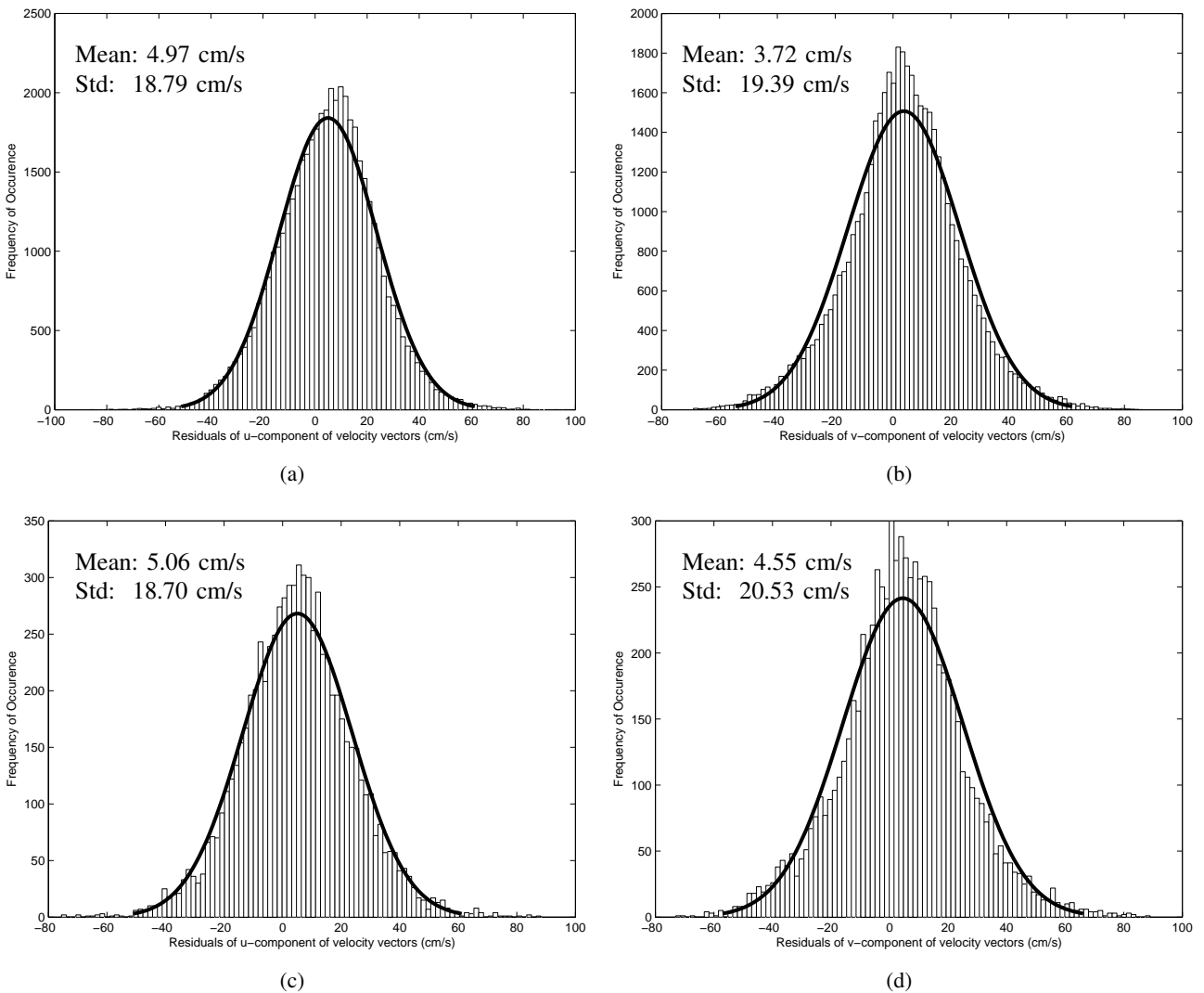


Fig. 10: Histograms of residuals for vector components of re-gridded MCC SAR currents. The top row is for the 2 km resolution HF radar currents, while the bottom row is for 6 km resolution HF radar currents. (a) and (c) are residual histograms for the u-component, (b) and (d) are residual histograms for the v-component. The thick black lines in are the normal histograms estimated from the mean and variance in the respective residuals. The mean and standard deviation for each case is indicated in the plots.

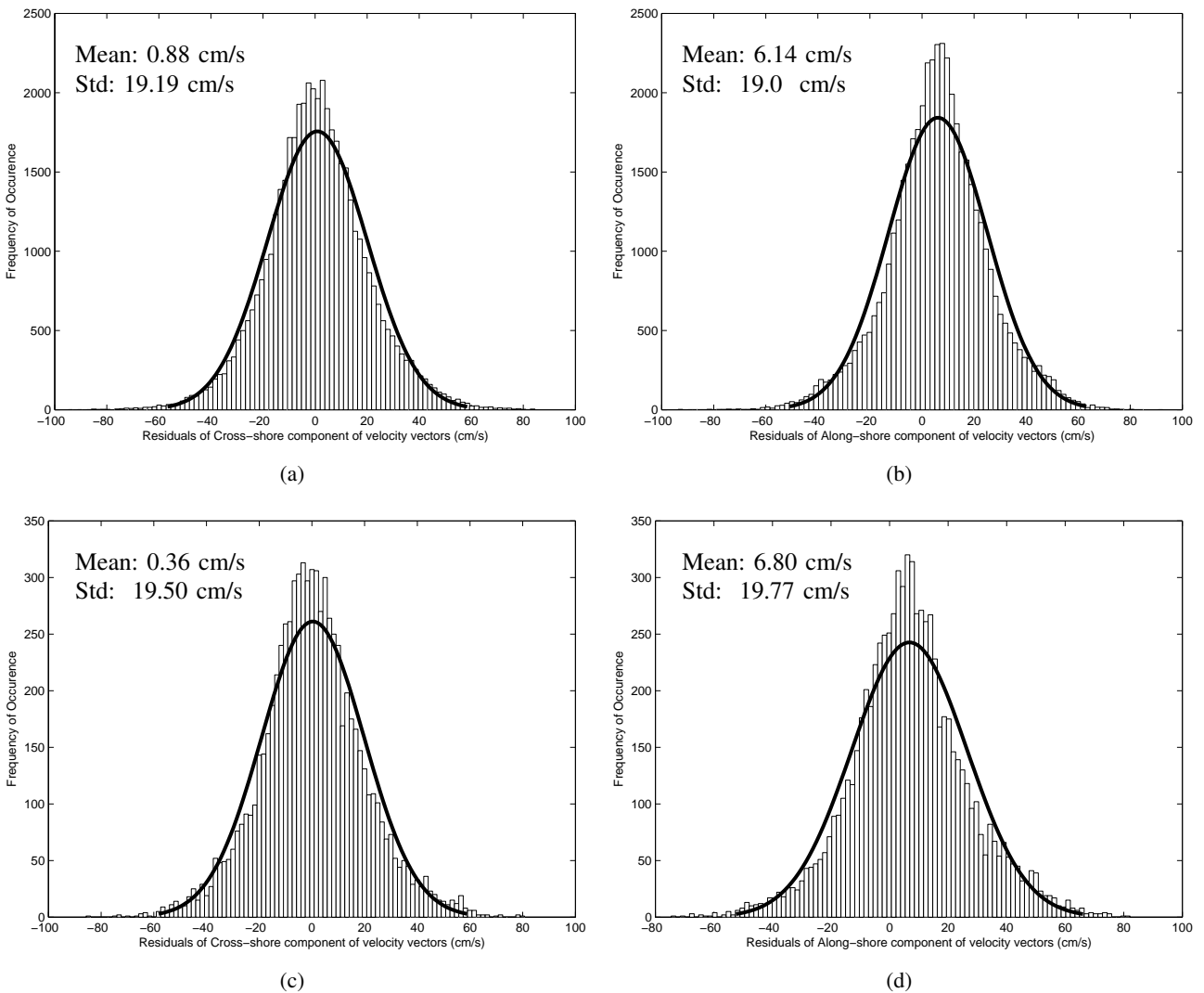


Fig. 11: Histograms of residuals for cross-shore and along-shore components of re-gridded MCC SAR currents. The top row is for the 2 km resolution HF radar currents, while the bottom row is for 6 km resolution HF radar currents. (a) and (c) are residual histograms for the cross-shore component, (b) and (d) are residual histograms for the along-shore component. The thick black lines in are the normal histograms estimated from the mean and variance in the respective residuals. The mean and standard deviation for each case is indicated in the plots.